Impact of 100 MeV Ag^{7+} SHI irradiation fluence and N incorporation on structural, optical, electrical and gas sensing properties of ZnO thin films

L. Balakrishnan[1] · S. Gokul Raj[2] · S. R. Meher[1] · K. Asokan[3] · Z. C. Alex[4]

Abstract   In the present study, we have investigated the influence of Ag^{7+} ion irradiation fluence and N incorporation on structural, optical, electrical and gas sensing properties of ZnO thin films. The X-ray diffraction analysis reveals the retainment of ZnO wurtzite structure even at higher fluence irradiation with slight decrease in crystallinity. Photoluminescence and Hall effect measurement analysis showed an increase in density of defects for high ion fluence irradiation. Atomic force microscope analysis shows that the films irradiated at high ion fluence have vertical standing needle-like morphology and also have high value of roughness compared with the films irradiated at low ion fluence. The ammonia and methanol gas sensing properties of the films have been studied at different operating temperature and gas concentration. It conveys that the films have selectivity towards ammonia than methanol and also that the films irradiated at high ion fluence exhibit better sensitivity, low response and recovery times compared with the films irradiated at low ion fluence. The film grown in oxygen ambience and irradiated at high ion fluence showed good sensing characteristics at all temperatures even at room temperature.
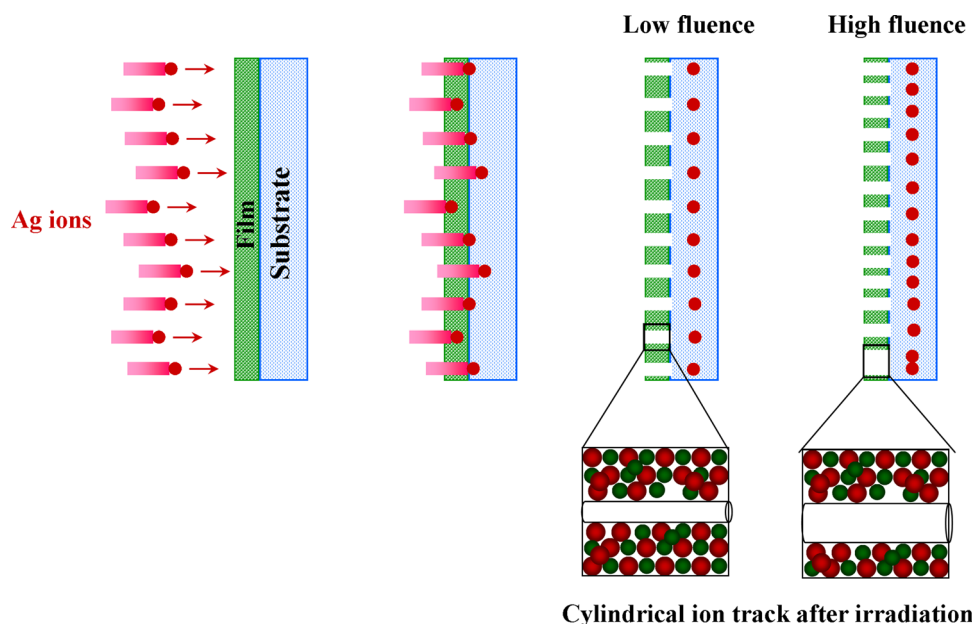
✉ L. Balakrishnan
bslv85@gmail.com

1   Materials Physics Division, School of Advanced Sciences, VIT University, Vellore 632 014, Tamil Nadu, India

2   Department of Physics, VEL Tech University, Avadi, Chennai 600 062, Tamil Nadu, India

3   Inter University Accelerator Centre, Aruna Asaf Ali Marg, New Delhi 110 067, India

4   MEMS and Sensor Division, School of Electronics Engineering, VIT University, Vellore 632 014, India

1 Introduction

In the recent past, modification of structural, optical, morphological and electrical transport properties of thin films towards different applications by means of high-energy relativistic particles (electron/proton), γ-rays and swift heavy ion (SHI) irradiation has received great attention [1, 2]. The modification depends on the ion species, ion energy and fluence [3]. The irradiation may cause displacement of atoms from their sites, creation of defects and ionization and/or excitation [4].

Among the different techniques, ion irradiation is an innovative and powerful tool in various fields of research such as synthesis of nanostructural thin films, structural phase transformation and surface and interface modification [1, 5–7]. It has also been well established that SHI irradiation can generate point defects and cylindrical defects, modify the local strain and dissolve the clusters [8–12]. Moreover, for sensor applications the surface–interface interaction between the test molecules and the sensing material is important. While SHI passes through the material, it produces perturbation in the electronic system of the target in a narrow cylinder along its trajectory. This narrow cylinder with a variety of defects leads to the change in microstructure and electronic transport properties, which plays a crucial role in gas sensing [13]. The size of this cylinder varies with the mass number of the irradiated ion and fluence. The scheme of SHI-induced effects in the film is depicted in Fig. 1.

When energetic ion beam penetrates through a material, the interaction is via two processes: one is direct transfer of energy to target atoms through elastic collisions, i.e. nuclear energy loss (S_n), and other is the electronic excitation/ionization of target atoms by inelastic collision, i.e. electronic energy loss (S_e). In SHI irradiation, the electronic

Fig. 1 Schematic representation SHI-induced modifications in thin films

Cylindrical ion track after irradiation

energy loss S_e due to inelastic collisions is several orders of magnitude higher than the nuclear energy loss S_n due to elastic collisions. The high S_e released by the ion beams in a very short interval of time produces significant excitation of the lattice, introducing defect levels that cause fundamental changes in the electronic structure and properties of the materials.

Recently, ZnO has attracted much scientific attention in the field of gas sensors due to its unique combination of properties such as high thermal stability, high chemical sensitivity, bio-compatibility, low cost, ease of availability and processing for sensor fabrication. However, the gas response for ZnO-based chemiresistive sensor is found to be low compared with the other commercial techniques such as gas chromatography and potentiometric and the enhancement in gas response is necessitated. Considerable improvements in the gas response of the sensor materials can be achieved (1) by adding dopants/catalysts, (2) by varying processing parameters or (3) by using post-deposition treatments such as annealing and ion irradiation. Currently, SHI irradiation is found to be a most powerful technique which can alter the properties of the material enormously as explained earlier [1, 14, 15]. Further, N is chosen as a dopant because it is an extensively studied dopant for ZnO in optoelectronics applications due to its similar ionic radii, low ionization energy and formation of shallow acceptor level [16–18]. But, here an attempt has been made to investigate the feasibility of choosing N as dopant for ZnO in gas sensor applications. SHI when traversing through ZnO thin films leads to a formation of different kinds of defects such as oxygen vacancies (V_O^{2+}), zinc interstitials (Zn_i^{2+}), zinc vacancies (V_{Zn}^{2-}), oxygen

interstitials (O_i^{2-}), zinc antisites (Zn_O^{2+}) and oxygen antisites (O_{Zn}^{2+}). Among the defects, V_O and Zn_i have low formation energy compared with the other defects. The kind of defects created during SHI irradiation can be examined through photoluminescence (PL) spectroscopy [19–21].

In this article, we have reported the influence of SHI fluence and N incorporation on structural, optical, electrical, morphological and gas sensing properties of ZnO thin films. The ammonia (NH_3) and methanol (CH_3OH) sensing mechanism, i.e. catalytic reaction process, has also been discussed in detail.

2 Experimental

2.1 Film growth

For irradiation, undoped and N-doped ZnO thin films of two different concentrations have been grown on Si (100) substrate by RF magnetron sputtering. The ZnO target for sputtering has been prepared by conventional solid-state reaction route. The process involves calcination of pure ZnO powder followed by pelletizing it into a circular disc of 2 in. diameter using hydraulic pelletizer through applying a pressure of 1.5 MPa. Then, it has been sintered at 950 °C for densification. The silicon substrate has been cleaned ultrasonically by successive rinsing in ethanol, acetone and distilled water; then, it has been dried by blowing hot air. Thus, prepared target and substrate have been loaded into the sputtering chamber at a distance of separation, 5 cm. The undoped and N-doped ZnO thin films of two different concentrations have been prepared by

varying the growth ambience (i.e. N_2 partial pressure). The O_2 and N_2 partial pressure used for the growth of three different films are 1. $O_2 = 0.01$ mbar, 2. O_2 + $N_2 = 0.01$ mbar with $O_2 = 0.005$ mbar and N_2 = 0.005 mbar and 3. $N_2 = 0.01$ mbar. The above-said partial pressures have been maintained during the film growth in an initially evacuated chamber to a base pressure of 8×10^{-6} mbar. All the films have been grown at a constant partial pressure, sputtering power and sputtering time of 0.02 mbar, 100 W and 30 min, respectively. The thickness of the films has been measured as approximately 150 nm by Filmetrics F20 in reflectance mode.

2.2 Irradiation

The undoped and N-doped ZnO thin films grown on Si (100) substrate have been irradiated with 100 MeV Ag^{7+} SHI. Two identical films of 1×1 cm^2 area grown with the above-mentioned parameters have been mounted on a ladder and placed in an irradiation chamber. The films have been irradiated with Ag^{7+} ions with two different fluences of 3×10^{10} and 3×10^{13} ions/cm^2 using the 15UD Pelletron tandem accelerator at Inter University Accelerator Centre, New Delhi. Irradiation was performed at a low angle with respect to the ion beam to avoid the channelling effect. The ion beam of ~1 mm diameter size was focused and scanned over the area of 1 cm^2 uniformly using magnetic scanners. The chamber vacuum range and beam current have been maintained as 10^{-6} Torr and 1 pnA (particle nanoampere), respectively. Since the projectile range is greater than the film thickness, most of the Ag ions are expected to fully penetrate through the film and no ions were implanted into the film. Hence, the modification was expected only due to the defects produced by the passage of ions through the film, so that SHI creates uniformly distributed defects such as cylindrical defects, point defects and lattice strain across the film thickness and area.

2.3 Characterization

The structural properties of the films have been studied using Rigaku Ultima III Max X-ray diffractometer with the K$_\alpha$ X-rays from the Cu target of wavelength 1.5406 Å in Bragg–Brentano geometry (θ/2θ coupled). The X-ray diffraction (XRD) pattern has been recorded in the range of 20°–80° for all samples. The electrical properties of the films have been measured by Ecopia HMS 3000 van der Pauw Hall effect measurement system at room temperature (RT). The Hall effect measurement has been repeated several times for each sample with different current values to check the consistency of the results. In order to analyse the defect levels and optical properties of the samples, PL measurement has been carried out with Varian Cary

Eclipse spectrometer using xenon lamp of wavelength 325 nm as an excitation source. The surface morphology was probed using Nanosurf Easy Scan 2 atomic force microscope over the scan area of 6×6 μm^2 in contact mode. The roughness parameters were estimated by analysing the X and Y axes topography scans of the film surfaces using Nanosurf software.

Gas sensing characteristics of irradiated ZnO films were studied for NH_3 and CH_3OH in an indigenously designed sensing set-up with sample heating arrangement. The electrical connections were made using fine copper wires with the film through conducting silver paste. The required gas concentration in the system is achieved by injecting a known volume of the NH_3 and CH_3OH gas from the calculated amount of compressed liquid NH_3 and CH_3OH. The resistance of the film has been measured using Keithley 6517A high resistance source meter. The electrical resistance of the films in air (R_a) and in the presence of gas (R_g) ambience is measured to evaluate the gas response, S (i.e. measure of sensitivity to gas adsorption), based on the following formula [22],

$$S (\%) = \frac{\left| R_g - R_a \right|}{R_a} \times 100 \tag{1}$$

The NH_3 and CH_3OH sensing response of the films were measured as a function of measurement time upon exposing the film to gas and atmosphere to obtain the sensing response, i.e. response kinetics (response and recovery time) of the sensing film. The response time is the time interval over which the resistance attains a saturated (final) value while the sensor is exposed to the target gas. Likewise, the recovery time is the time interval over which the sensor resistance reduced to ~10 % of the saturated value while the sensor is exposed to the atmosphere.

3 Results and discussion

3.1 Structural analysis

Figure 2 shows the XRD pattern of Ag ions irradiated ZnO films (of different N concentration) with low and high fluences. In all the films, only two peaks have been observed, a peak observed around ~34.4° corresponds to (0002) diffraction plane of ZnO and a peak around ~69.2° corresponds to the silicon substrate. It implies that all the films have polycrystalline hexagonal wurtzite structure with c-axis, i.e. (0002) preferred orientation perpendicular to the substrate surface due to the less surface free energy of (0002) plane [23]. From the figure, it is interesting to observe that the (0002) peak intensity of all the films irradiated at high fluence decreases. It could be attributed to the creation of defects such as ion tracks (i.e. cylindrical
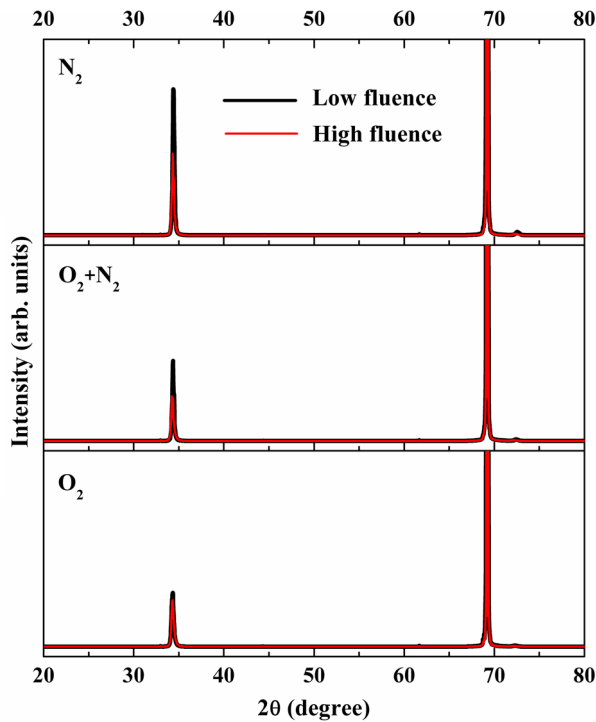
Fig. 2 XRD pattern of ZnO films grown in different ambience with low and high ion fluence irradiation

voids perpendicular to the substrate surface) which dominates over the thermal spike-induced crystallization process [24–26]. Further, the crystalline quality increases with the increase in N concentration in both low and high fluence irradiation. The increase in crystallinity with the increase in N concentration is due to the decrease in density of defects (such as oxygen vacancies) compared with the undoped ZnO film during the film growth.

The parameters such as full width at half maximum (FWHM), stress, microstrain, dislocation density and number of crystallites per unit area have also been calculated and are summarized in Table 1. FWHM has been determined using Gaussian function to approximate the line shapes of the fitting components, and raw experimental data have been used for fitting without preliminary

smoothing. The FWHM of all the films irradiated at high fluence is high compared with the films irradiated at low fluence due to the formation of more defects thereby reduces crystallinity. Further, the decrease in FWHM with increase in N concentration in both the cases is due to the improvement of stoichiometry by the incorporation N atoms and decrease in density of defects. In the case of films grown in the presence of N_2, the free energy of formation of O vacancies is reduced because of the high electronegativity of N^{3-} ions in O^{2-} site. This leads to the improvement in crystallinity for the films grown in N_2 ambience compared with the film grown in O_2 ambience.

The grain (crystallite) size (D) of the film has been calculated using the Scherrer's formula [27],

$$D = \frac{K\lambda}{\beta \cos\theta} \tag{2}$$

where K is the shape factor that varies from 0.89 (for spherical) to 0.94 (for cubic). Usually, this value is set as 0.9 for crystallites of unknown shape, λ is the X-ray wavelength, β is the FWHM in radians, and θ is the Bragg's angle.

The stress (σ) in the film has been calculated from the following relation [28],

$$\sigma = \left[2C_{13} - \frac{(C_{11} + C_{12})C_{33}}{C_{13}} \right] \times \frac{c - c_0}{c_0} \tag{3}$$

where the elastic stiffness constants are given as $C_{11} = 208.8$ GPa, $C_{33} = 213.8$ GPa, $C_{12} = 119.7$ GPa and $C_{13} = 104.2$ GPa [27].

By substituting above values, it gives the following numerical relation for the stress,

$$\sigma = -233 \times \frac{c - c_0}{c_0} \text{ (GPa)} \tag{4}$$

where c is the lattice parameter of ZnO calculated from (0002) peak of XRD pattern and c_0 is the lattice parameter of unstressed bulk ZnO (5.206 Å).

From the table, it is seen that all the films in both the cases have compressive stress due to formation of cylindrical ion tracks; accordingly, the forces that act in the

Table 1 Thin film parameters calculated from XRD analysis

Ion fluence	Growth ambience	FWHM (°)	σ (GPa)	Microstrain (× 10^{-4} rad.)	Dislocation density (× 10^{14} lines/m²)	N (× 10^{14}/m²)
Low fluence	O_2	0.299	−0.694	12.466	15.867	94.800
	$O_2 + N_2$	0.251	−0.371	10.463	11.184	56.106
	N_2	0.241	−0.055	10.045	10.314	49.683
High fluence	O_2	0.333	−0.971	13.885	19.676	130.919
	$O_2 + N_2$	0.323	−0.766	13.467	18.515	119.505
	N_2	0.315	−0.694	13.133	17.611	110.853

planes of the film causes increase in lattice spacing. Further, the increase in stress for the films irradiated at high fluence is due to the formation of more/wide cylindrical ion tracks; consequently, the tensile forces that act in the planes increases.

The microstrain, dislocation density and number of crystallites per unit area were calculated using the following relations [29–31],

$$\text{Microstrain} \ (\varepsilon) = \frac{\beta \cos \theta}{4} \tag{5}$$

$$\text{Dislocation density} \ (\delta) = 1/D^2 \tag{6}$$

$$\text{Number of crystallites per unit area} \ (N) = t/D^3 \tag{7}$$

where β is the FWHM, D is the crystallite size, θ is the peak position, and t is the thickness of the film. It is seen that for the films irradiated at high fluence the microstrain, dislocation density and number of crystallites per unit area increase compared with the films irradiated at low fluence. The increase in dislocation density is due to the formation of more/wide cylindrical ion tracks; thereby, microstrain in the film increases due to the increase in tensile force on the planes. Further, irradiation of films by SHI imparts enormous energy to the film; consequently, the high lattice vibration and defects formation lead to the grain splitting [32, 33]. Hence, the number of crystallites per unit area increases for the films irradiated with high ion fluence.

Further, it has been noticed that the films are not amorphized even at high fluence irradiation. Hence, the films could also be used in the radiation-harsh environment for various gas sensor applications.

3.2 Optical analysis

Figure 3a and b shows the room temperature PL spectra of the ZnO films irradiated with Ag ions of low and high fluences. The spectrum has been resolved into its constituent bands to observe clear variation using Gaussian function. All the films showed UV emission at around 366–390 nm due to free exciton recombination and two broad deep-level emissions around 450 and 500 nm related to the structural defects. The presence of intense and broad deep-level emissions are attributed to the formation of more structural defects such as V_O, Zn_i, V_{Zn} and O_i through the creation of cylindrical tracks by the passage of energetic ions. Figure 3c shows the schematic band diagram of the location of defect levels and their corresponding radiative emission wavelength ranges constructed from the experimental and theoretical investigations. Here, instead of well-defined peaks, PL reveals broad deep-level emissions. The defect level emissions nearby in wavelength are very much competitive due to heavy ion impact and finally merged into a single well-developed peak.

The broad green band emission around 500 nm is primarily attributed to the transition from $V_O \rightarrow VB$. The broadness of the peak is due to the few of other defects such as oxygen interstitial (O_i) and oxygen antisite (O_{Zn}). Similarly, one more broad defect-related emission (blue band) around 450 nm is assigned to the recombination of electron from CB to the shallow level defect, zinc vacancy (V_{Zn}) [19]. Likewise, the broadness of the peak is due to the presence of few other shallow level defects such as zinc interstitial (Zn_i). Table 2 shows the variation of near band edge (NBE) emission energy, and intensity ratios of I_{NBE}/I_{BB} and I_{NBE}/I_{GB} (where I_{NBE}, I_{BB} and I_{GB} are the intensities of NBE, i.e. UV, blue band and green band emissions, respectively) as a function of growth ambience and ion fluence. The relative intensity ratio between NBE to deep-level emissions such as I_{NBE}/I_{BB} and I_{NBE}/I_{GB} is usually employed to characterize the crystalline quality [34]. The larger intensity ratio indicates that the films have better crystallinity, i.e. less defects. From the table, it is seen that the NBE emission energy increases with the increase in N_2 ambience due to the substitution of N atoms on O sites. This leads to the decrease in electron concentration; thereby, the NBE emission wavelength varies according to Burstein–Moss effect (electron concentration α $1/\lambda$) [35]. Further, the emission wavelength of the films irradiated at high fluence are low compared with the films irradiated at low fluence due to the presence of high concentration of defects, which leads to the creation of more electrons. This has been reflected in I_{NBE}/I_{BB} and I_{NBE}/I_{GB} values as the increase in number with N_2 ambience and decrease at high ion fluence. These results are in accord with the XRD results.

3.3 Electrical analysis

Table 3 shows the Hall measurement results of all the films irradiated at low and high ion fluences. It has been observed that the electron concentration of the films irradiated at high fluence is high compared with the films irradiated at low fluence. This is due to the formation of more donor-like defects such as V_O and Zn_i due the ion passage. When the SHI passes through the solid, the higher electronic stopping of ions can weaken oxygen bonds in the ZnO, resulting in the formation of V_O and Zn_i [36]. In the case of film grown in O_2 ambience, the electron concentration increases. As the film grows in $O_2 + N_2$ ambience, the hole concentration decreases due to the formation of donor defects; thereby, the film irradiated at high ion fluence shows oscillatory behaviour between p- and n-type conductivity. Similarly, as the film grows in N_2 ambience the hole concentration decreases at high ion fluence irradiation. It has been seen that the mobility of films increases with increase in N_2 partial pressure in both the cases
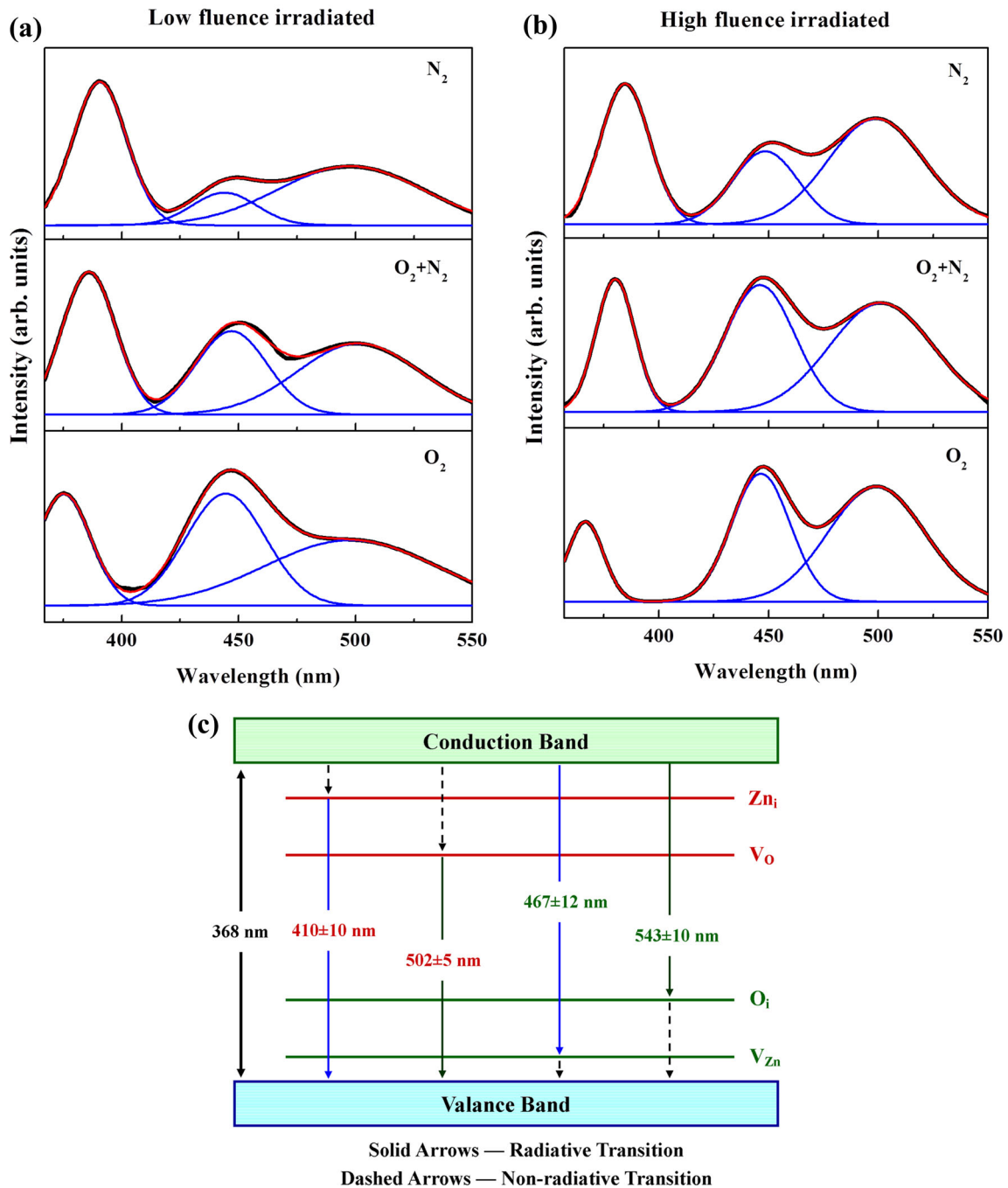
Fig. 3 PL spectra of ZnO films grown in different ambience with **a** low fluence and **b** high fluence ion irradiation. **c** Schematic energy band diagram with defect levels

because of decrease in concentration of defects due to the substitution of N atoms [37, 38]. In addition, the mobility of the films irradiated at high fluence is low compared with the films irradiated at low fluence due to the presence of more defects. Thus, the Hall effect measurement results are well acknowledged by XRD and PL analysis.

3.4 Morphology analysis

Besides the structural modification, the SHI irradiation also tailors the surface microstructure through the formation cylindrical ion tracks. This change in surface microstructure improves the gas sensing properties of the thin film

Table 2 Variation of NBE emission energy

Growth ambience	Low fluence			High fluence		
	NBE wavelength (nm)	I_{NBE}/I_{BB}	I_{NBE}/I_{GB}	NBE wavelength (nm)	I_{NBE}/I_{BB}	I_{NBE}/I_{GB}
O_2	374.9	1	1.96	366.5	0.63	0.70
$O_2 + N_2$	385.8	1.64	2.21	380.0	1.05	1.22
N_2	390.4	6.49	2.81	384.5	2.02	1.35

Table 3 Electrical properties of all the films irradiated at low and high ion fluence

Growth ambience	Low fluence		High fluence	
	Carrier concentration (cm^{-3})	Mobility (cm^2/Vs)	Carrier concentration (cm^{-3})	Mobility (cm^2/Vs)
O_2	$-(5.4 \pm 3.1) \times 10^{18}$	$(3.6 \pm 2.7) \times 10^{-1}$	$-(2.8 \pm 2.6) \times 10^{19}$	$(7.2 \pm 3.2) \times 10^{-2}$
$O_2 + N_2$	$+(1.2 \pm 2.8) \times 10^{16}$	$(6.5 \pm 3.9) \times 10^{1}$	$\pm (2.4 \pm 1.9) \times 10^{15}$	$(5.8 \pm 4.1) \times 10^{0}$
N_2	$+(7.1 \pm 1.9) \times 10^{17}$	$(4.1 \pm 1.6) \times 10^{2}$	$+(9.4 \pm 3.8) \times 10^{15}$	$(5.5 \pm 2.3) \times 10^{1}$

[39]. Therefore, to further probe the surface microstructures of the films, AFM measurements were taken. Figure 4 shows the 3D surface microstructure of the films irradiated at low and high ion fluences. All the films irradiated at high ion fluence showed vertical standing needle-like structure due to the passage of high concentration of heavy ions through the film. The films irradiated at high ion fluence are found to be highly porous compared with the films irradiated at low fluence. Thus, the increase in surface area for catalytic reaction in the case of films irradiated at high ion fluence may lead to the increase in gas sensitivity. The films irradiated at low ion fluence showed the root mean square (rms) roughness values of 77.12, 30.27 and 11.75 nm, and the films irradiated at high ion fluence showed roughness values of 254.8, 192.5 and 125.3 nm. It has been seen that the films irradiated at high ion fluence showed higher value of roughness compared with the films irradiated at low ion fluence due to the formation of more defects. Further, the roughness of the films decreases with the increase in N_2 ambience in the growth in both case of irradiation (high and low ion fluence) which is due to the decrease density of native defects.
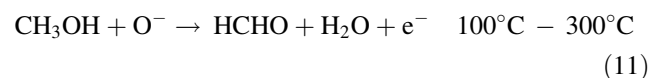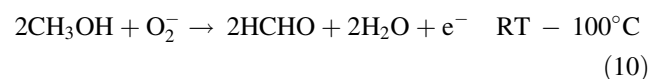
3.5 Gas sensing mechanism

Generally, the gas sensing of oxide materials is explained by oxygen adsorption model [40]. According to this model, oxygen atoms from the ambient atmosphere are chemisorbed on the surface of the material which traps the electrons from conduction band. While exposure to a reducing gas, those chemisorbed oxygen undergoes surface reactions, which leads to the release of trapped electrons. In case of n-type semiconductor, release of electrons causes increase in the electron concentration, which leads to the decrease in resistance. For p-type semiconductor, this phenomenon is vice versa, i.e. the release of electrons through surface reactions causes recombination as the majority carriers are holes, resulting in a decrease in hole concentration and increase in resistance. The stable oxygen ions which are responsible for the surface reactions upon exposure to target gas are O_2^- (below 100 °C) and O^- (100–300 °C) [41]. Hence, the possible reactions which alter the film resistance are as follows,

$$4NH_3 + 3O_2^- \rightarrow 2N_2 + 6H_2O + 3e^-, \quad RT - 100°C \tag{8}$$

$$2NH_3 + 3O^- \rightarrow N_2 + 3H_2O + 3e^-, \quad 100°C - 300°C \tag{9}$$

Similarly,

$$2CH_3OH + O_2^- \rightarrow 2HCHO + 2H_2O + e^- \quad RT - 100°C \tag{10}$$

$$CH_3OH + O^- \rightarrow HCHO + H_2O + e^- \quad 100°C - 300°C \tag{11}$$
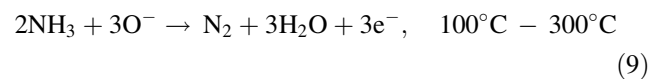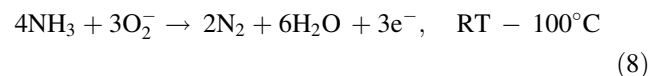
From the above redox processes, it is seen that at elevated temperatures less number of gas molecules are sufficient to release the same number of electrons compared with room temperature. Moreover, at elevated temperatures, because of thermal energy the whole reaction process would be prompted by the high activation energy [42]. Hence, there has been higher sensitivity at elevated temperatures.

Further, few of the oxygen species in the regular sites also undergoes catalytic reaction that has been explained by the following competitive reactions [43],
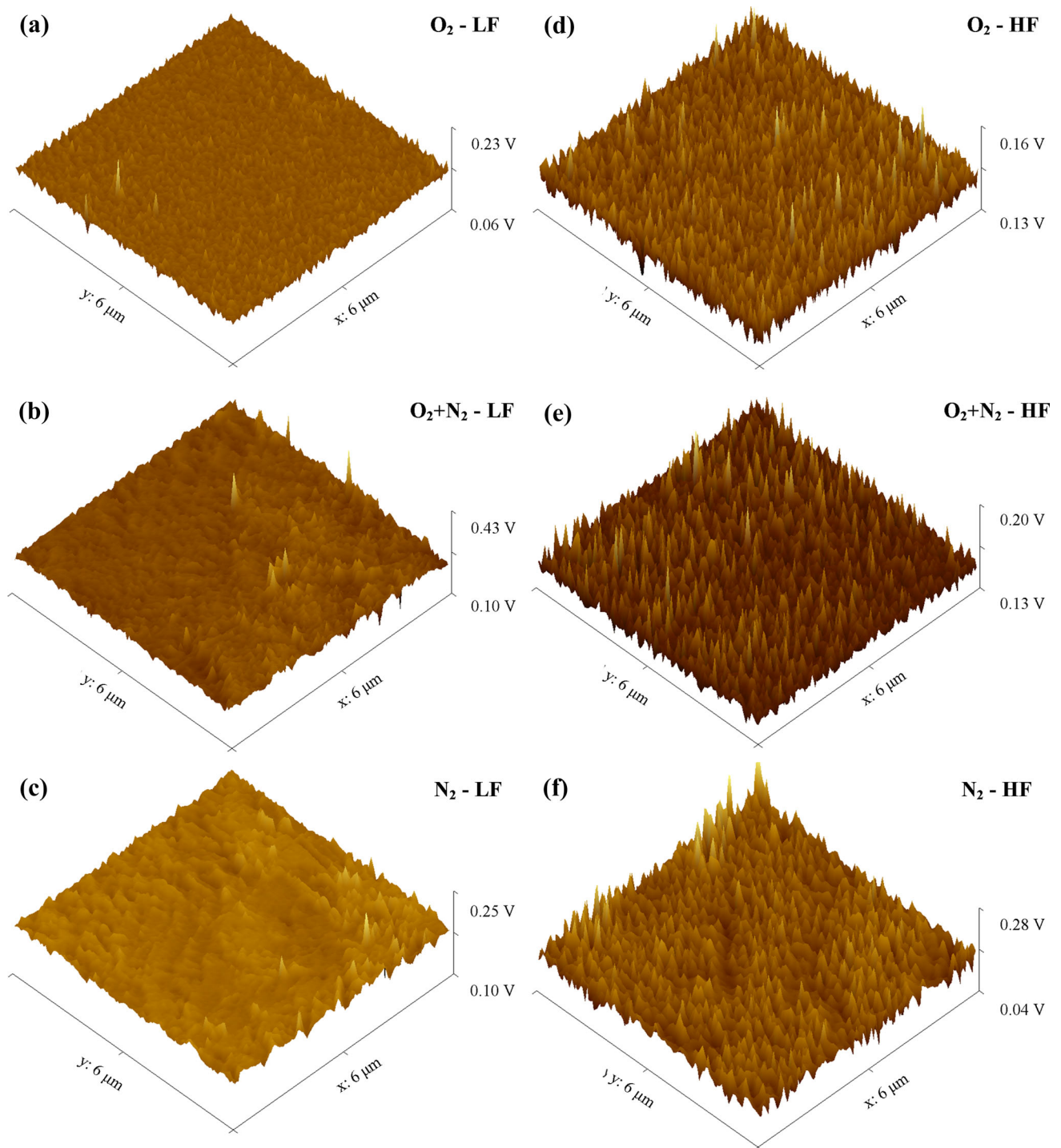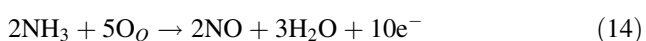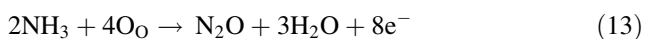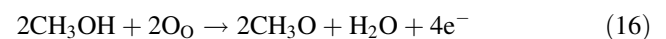
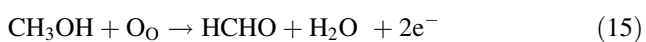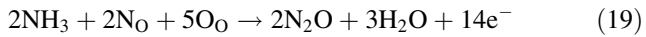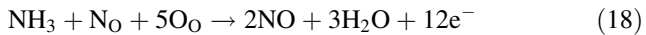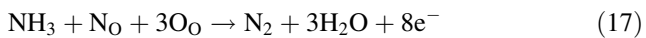$$2NH_3 + 3O_O \rightarrow N_2 + 3H_2O + 6e^- \tag{12}$$
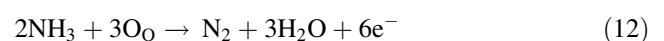
Fig. 4 **a**, **b** and **c** are the AFM images of all the films grown in different ambience and irradiated with low ion fluence, and **d**, **e** and **f** are the AFM images of all the films grown in different ambience and irradiated with high ion fluence
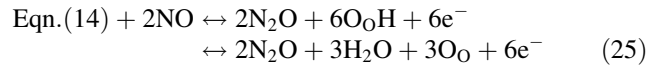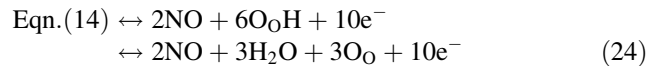
$$2NH_3 + 4O_O \rightarrow N_2O + 3H_2O + 8e^- \qquad (13)$$

$$2NH_3 + 5O_O \rightarrow 2NO + 3H_2O + 10e^- \qquad (14)$$

Similarly,

$$CH_3OH + O_O \rightarrow HCHO + H_2O + 2e^- \qquad (15)$$

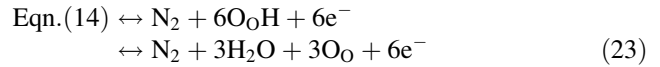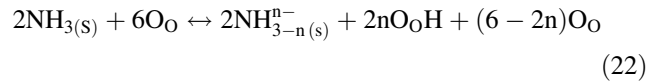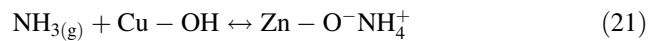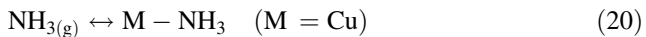$$2CH_3OH + 2O_O \rightarrow 2CH_3O + H_2O + 4e^- \qquad (16)$$

where O_O is the lattice oxygen in the regular site. Similarly, there is some possibility for the catalytic reaction of nitrogen atoms substituted in oxygen sites (N_O) in addition to O_O. The reactions are

$$NH_3 + N_O + 3O_O \rightarrow N_2 + 3H_2O + 8e^- \quad (17)$$

$$NH_3 + N_O + 5O_O \rightarrow 2NO + 3H_2O + 12e^- \quad (18)$$

$$2NH_3 + 2N_O + 5O_O \rightarrow 2N_2O + 3H_2O + 14e^- \quad (19)$$

But, nitrogen in the regular lattice site (N_O) cannot react directly with CH_3OH but undergoes indirect reaction through O_O with very low probability. Hence, those reactions will not play a dominant role in determining the resistance of the film.

In the case of NH_3 gas sensing, there are several intermediate species and reaction pathways are involved which may differently affect the sensor response. The whole process has been described as follows,

$$NH_{3(g)} \leftrightarrow M - NH_3 \quad (M = Cu) \quad (20)$$

$$NH_{3(g)} + Cu - OH \leftrightarrow Zn - O^-NH_4^+ \quad (21)$$

$$2NH_{3(S)} + 6O_O \leftrightarrow 2NH_{3-n\,(s)}^{n-} + 2nO_OH + (6-2n)O_O \quad (22)$$

$$Eqn.(14) \leftrightarrow N_2 + 6O_OH + 6e^- \\ \leftrightarrow N_2 + 3H_2O + 3O_O + 6e^- \quad (23)$$

$$Eqn.(14) \leftrightarrow 2NO + 6O_OH + 10e^- \\ \leftrightarrow 2NO + 3H_2O + 3O_O + 10e^- \quad (24)$$

$$Eqn.(14) + 2NO \leftrightarrow 2N_2O + 6O_OH + 6e^- \\ \leftrightarrow 2N_2O + 3H_2O + 3O_O + 6e^- \quad (25)$$

As reported by Jimenez et al. [44], in the catalytic reaction, NH_3 molecules can be adsorbed on acidic Lewis and Brønsted sites. If NH_3 is not simply desorbed, it forms
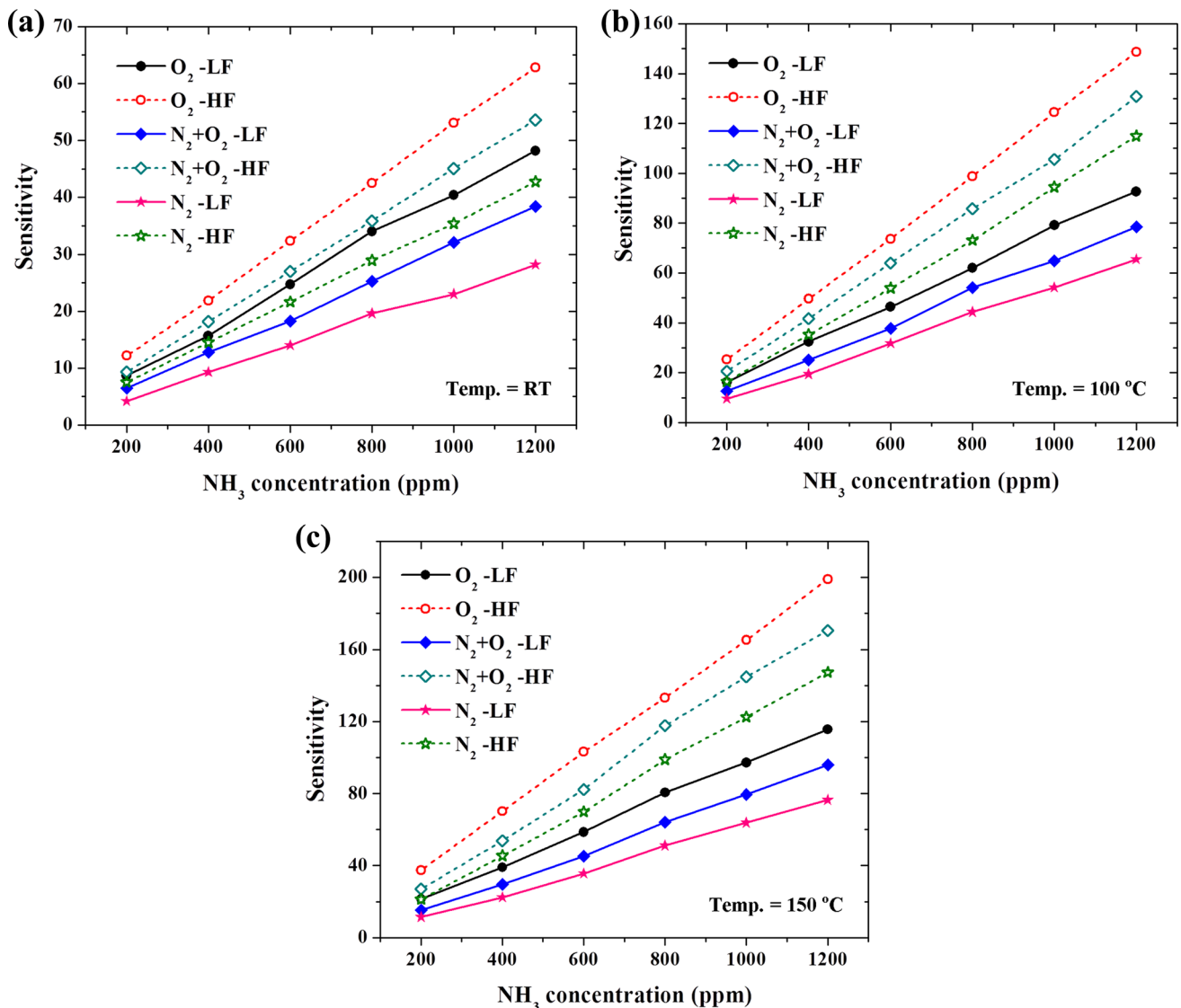

Fig. 5 Ammonia gas sensing characteristics of the films at **a** RT, **b** 100 °C and **c** 150 °C. *Solid lines* low fluence (LF) irradiated and *dotted lines* high fluence (HF) irradiated

hydroxyl groups by dehydrogenation through hydrogen capture by oxygen centres (Eq. 9). It gives NH_{3-n}^{n-} species (Eq. 10) which are no longer desorbed, and they can interact with another NH_{3-n}^{n-} species which forms molecular nitrogen (Eq. 11). Otherwise, in the oxygen atmosphere, they react with a chemisorbed or lattice oxygen and forms nitrogen monoxide (Eq. 12). Also, NH_{3-n}^{n-} species react with nitrogen monoxide and forms nitrous oxide (Eq. 11). In the case of CH_3OH sensing, also there will be more possibility for the second-order reactions with different reaction pathways that have been explained as follows,

$$2CH_3OH + O_2^- \rightarrow 2HCHO + 2H_2O + e^- \text{ and } 2HCHO + O_2^-$$
$$\rightarrow 2HCOOH + e^- \text{ and } HCHO + O_2^-$$
$$\rightarrow H_2O + CO_2 + e^-$$

(26)

$$CH_3OH + O^- \rightarrow HCHO + H_2O + e^- \text{ and } HCHO + O^-$$
$$\rightarrow HCOOH + e^- \text{ and } HCHO + 2O^-$$
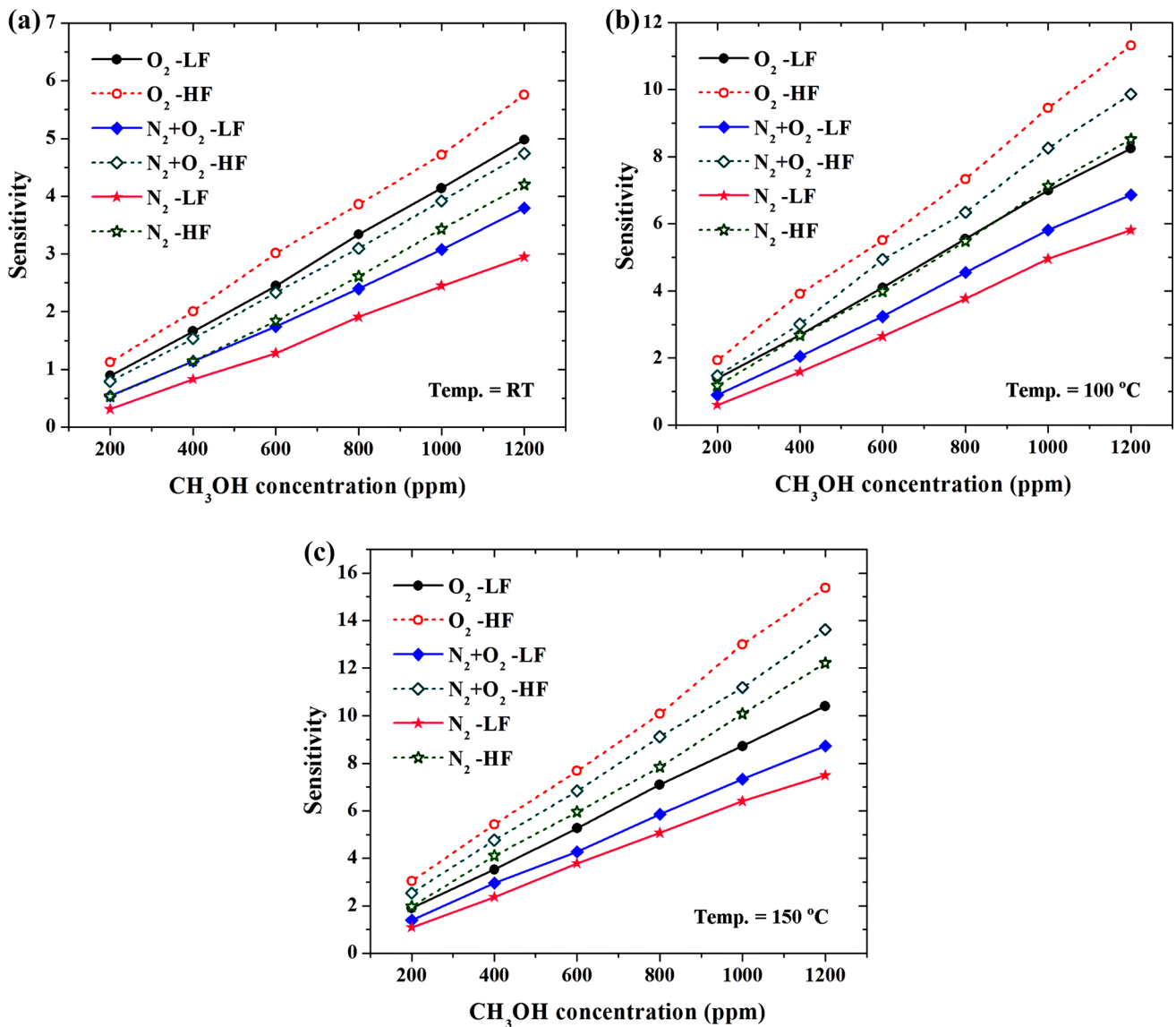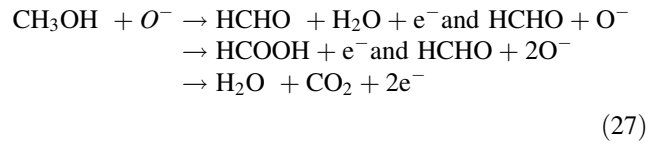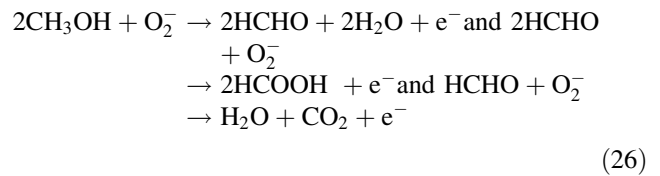$$\rightarrow H_2O + CO_2 + 2e^-$$

(27)

Fig. 6 Methanol gas sensing characteristics of the films at **a** RT, **b** 100 °C and **c** 150 °C. *Solid lines* low fluence (LF) irradiated and *dotted lines* high fluence (HF) irradiated
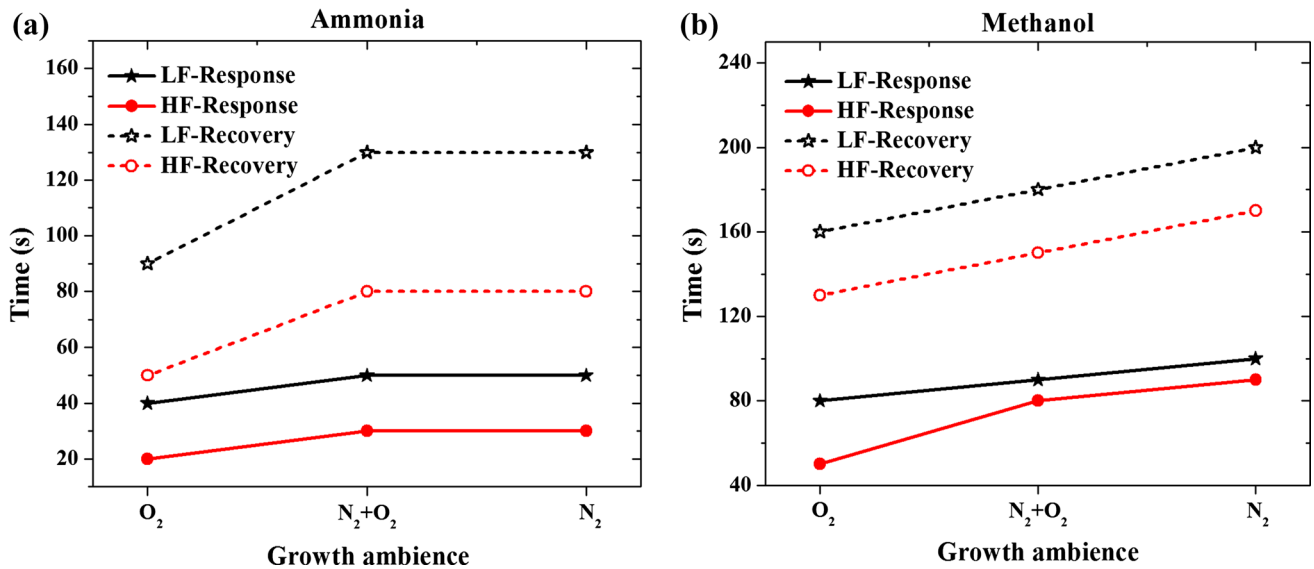
Fig. 7 Response and recovery times of all the films irradiated at low and high ion fluence for **a** ammonia and **b** methanol at room temperature. *Solid lines* response time and *dotted lines* recovery time
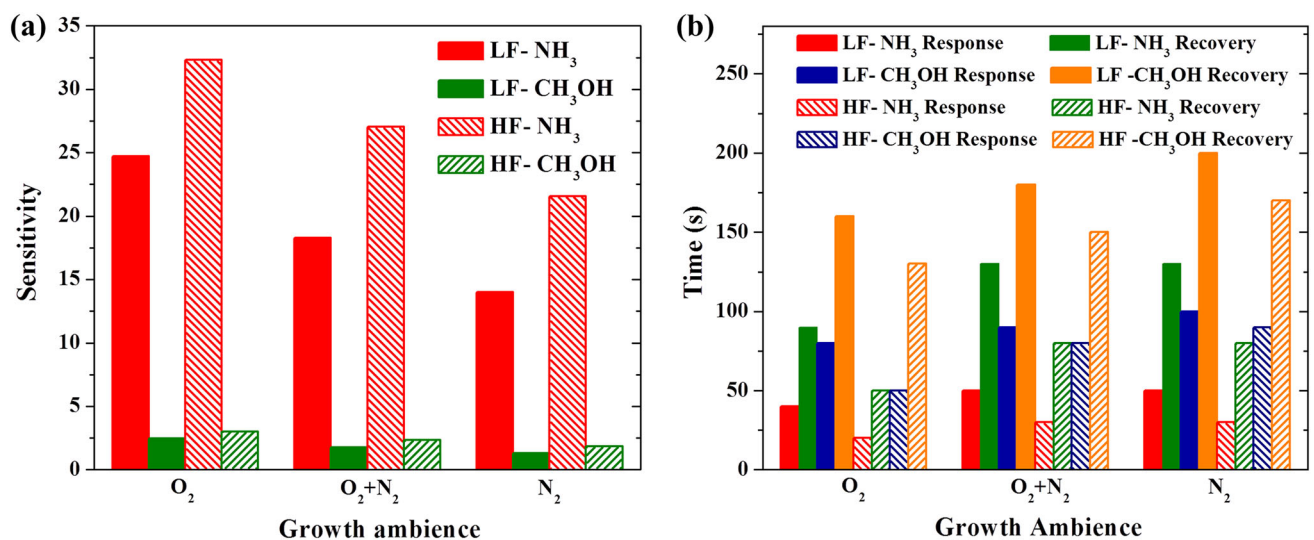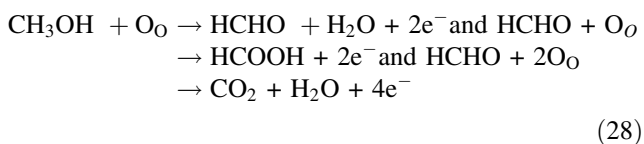

Fig. 8 a Sensitivity and **b** response kinetics comparison bar chart of all the films for both NH$_3$ and CH$_3$OH methanol at room temperature

$$CH_3OH + O_O \rightarrow HCHO + H_2O + 2e^- \text{ and } HCHO + O_O$$
$$\rightarrow HCOOH + 2e^- \text{ and } HCHO + 2O_O$$
$$\rightarrow CO_2 + H_2O + 4e^-$$

$$(28)$$

Thus, in one way CH$_3$OH is oxidized to formaldehyde and subsequently into formic acid. In another way, CH$_3$OH is oxidized to formaldehyde and into carbon dioxide [45].

As a result, the electrons generated on the surface of the film through any of the reaction pathways will be responsible for the gas sensing mechanism in the case of metal oxides.

3.6 Gas sensing

The sensitivity factor 'S' has been determined for all the films irradiated at low and high fluences at different NH$_3$ and CH$_3$OH concentrations (200, 400, 600, 800, 1000 and 1200 ppm) and operating temperatures (RT, 100 and 150 °C) using Eq. 1. Figure 5a, b and c and Fig. 6a, b and c show the NH$_3$ and CH$_3$OH sensing characteristics for both kinds of films irradiated at low and high fluences at different operating temperatures. It has been seen that all the films showed linear raise in sensitivity with NH$_3$ and CH$_3$OH concentrations. All the films irradiated at high

fluence showed enhanced sensitivity compared with the films irradiated at low fluence. This is due to the formation of more/wide cylindrical ion tracks by the passage of high fluence ions, which thereby increases the surface area for gas interaction. The sensitivity of all the films increases with the increase in operating temperature due to the increased catalytic reaction at the film surface. The film grown in O_2 ambience showed better sensitivity due to the presence of more defects compared with the films grown in $O_2 + N_2$ and N_2 ambience. Further, the sensitivity of the films decreases with the increase in N_2 ambience, which is due to the decrease in density of defects such as V_O and Zn_i. It has been noticed that both the films grown in O_2 ambience irradiated at low and high fluences showed better sensitivity at room temperature.

The response and recovery times of all the films irradiated at low and high fluences have been determined by observing the change in sensitivity of the films as a function of time upon exposure to target gas and air ambience, respectively. Figure 7a and b shows the response kinetics of all the films for 600 ppm of NH_3 and CH_3OH at room temperature, respectively. It has been observed that the films irradiated at high fluence showed low response and recovery time compared with the films irradiated at low fluence for both NH_3 and CH_3OH. Further, the films grown in O_2 ambience showed low response and recovery time compared with the films grown in $O_2 + N_2$ and N_2 ambience for both kind of irradiation (low and high fluences). This is due to the presence of more defects and high catalytic activity of O atoms.

Figure 8a shows the room temperature sensitivity comparison bar chart of all the films for both NH_3 and CH_3OH. It implies that all the films irradiated at high fluence have better sensitivity compared with the films irradiated at low fluence. Further, it shows that all the films have better selectivity towards NH_3 than CH_3OH. The film grown in O_2 ambience and irradiated at high ion fluence showed better sensitivity. Similarly, Fig. 8b shows the room temperature response and recovery time comparison bar chart for all the films. It has been seen that all the films have low response and recovery times for NH_3 compared with CH_3OH. In addition, the films irradiated at high ion fluence have low response and recovery times compared with the films irradiated at low ion fluence. Compared to all the films, the film grown in O_2 ambience and irradiated at high fluence showed very low response and recovery time for NH_3. Hence, it has been concluded that this kind of irradiation approach will pave a way for the realization of room temperature chemiresistive NH_3 sensor which can even work in the radiation-harsh environment.

4 Conclusion

The undoped and N-doped ZnO films of two different concentrations have been prepared by growing the films in different atmospheres such as O_2, $O_2 + N_2$ and N_2 using RF magnetron sputtering. The effect of Ag ion irradiation fluence on the films has been studied by XRD, PL, Hall effect measurement, AFM and gas sensing. The XRD and PL analysis convey that upon irradiation with high ion fluence the crystallinity of the films decreases and the density of defect increases. Further, the Hall effect measurement results showed increase in electron concentration for the films irradiated with high ion fluence compared with the films irradiated with low fluence due to the formation more donor defects. The NH_3 and CH_3OH sensing studies imply that the films irradiated at high ion fluence have increased sensitivity ($\sim$ >ten times) and low response/recovery times compared with the low fluence irradiated one. This is due to the formation of cylindrical ion tracks which thereby increases the surface area for catalytic reaction. Further, all the films are selective towards NH_3 than CH_3OH and the film grown in O_2 ambience and irradiated at high ion fluence showed good sensitivity and low response/recovery times even at room temperature. Hence, it has been concluded that this method of SHI irradiation will be a splendour candidate for the realization of ZnO-based room temperature chemiresistive sensor.

References

1. D. Kanjilal, Curr. Sci. **80**, 1560 (2001)
2. W. Wesh, A. Kamarou, E. Wendler, Nucl. Instrum. Methods B **225**, 111 (2004)
3. D.K. Avasthi, Curr. Sci. **78**, 1297 (2000)
4. S.M. El-Sayed, Nucl. Instrum. Methods B **225**, 535 (2004)
5. S.P. Patel, S.A. Khan, A.K. Chawla, R. Chandra, J.C. Pivin, D. Kanjilal, L. Kumar, Phys. B **406**, 4150 (2011)
6. S.P. Patel, A.K. Chawla, R. Chandra, J. Prakash, P.K. Kulriya, J.C. Pivin, D. Kanjilal, L. Kumar, Solid State Commun. **150**, 1158 (2010)
7. D.K. Avasthi, J.C. Pivin, Curr. Sci. **98**, 780 (2010)
8. S. Khatua, P.K. Mishra, R. Kumar, D.C. Kundaliya, D. Buddhikot, R. Pinto, S.K. Malik, J. Appl. Phys. **96**, 7403 (2004)
9. R. Kumar, R.J. Choudhary, S.I. Patil, S. Husain, J.P. Srivastava, S.P. Sanyal, S.E. Lofland, J. Appl. Phys. **96**, 7383 (2004)
10. R.J. Choudhary, R. Kumar, S. Husain, J.P. Srivastava, S.I. Patil, S.K. Malik, Appl. Phys. Lett. **82**, 222501 (2005)
11. B. Angadi, Y.S. Jung, W.K. Choi, R. Kumar, K. Jeong, S.W. Shin, J.H. Lee, J.H. Song, M.W. Khan, J.P. Srivastava, Appl. Phys. Lett. **88**, 142502 (2006)

12. R. Kumar, M.W. Khan, J.P. Srivastava, S.K. Arora, R.G.S. Sofin, R.J. Choudhary, I.V. Shvets, J. Appl. Phys. **100**, 033703 (2006)
13. A.A. Sagade, R. Sharma, I. Sulaniya, J. Appl. Phys. **105**, 043701 (2009)
14. D.K. Avasthi, S. Ghosh, S.K. Srivastava, W. Assmann, Nucl. Instrum. Methods B **219–220**, 206 (2004)
15. R.R. Ahire, A.A. Sagade, N.G. Deshpande, S.D. Chavan, R. Sharma, F. Singh, J. Phys. D **40**, 4850 (2007)
16. J. Huang, S. Chu, J. Kong, L. Zhang, C.M. Schwarz, G. Wang, L. Chernyak, Z. Chen, J. Liu, Adv. Opt Mater. **1**, 179 (2013)
17. J.-F. Chien, H.-Y. Liao, S.-F. Yu, R.-M. Lin, M. Shiojiri, J.-J. Shyue, M.-J. Chen, A.C.S. Appl, Mater. Interfaces **5**, 227 (2013)
18. S.-L. Yao, J.-D. Hong, C.-T. Lee, C.-Y. Ho, D.-S. Liu, J. Appl. Phys. **109**, 103504 (2011)
19. A. Janotti, C.G.V. Walle, Rep. Prog. Phys. **72**, 126501 (2009)
20. K. Vanheusden, W.L. Warren, C.H. Seager, D.R. Tallant, J.A. Voigt, B.E. Gnade, J. Appl. Phys. **79**, 7983 (1996)
21. Y.-J. Lin, C.-L. Tsai, Y.-M. Lu, C.-J. Liu, J. Appl. Phys. **99**, 093501 (2006)
22. M. Kaura, N. Jain, K. Sharma, S. Bhattacharya, M. Roy, A.K. Tyagi, S.K. Gupta, J.V. Yakhmi, Sens. Actuators, B **133**, 456 (2008)
23. N. Fujimura, T. Nishihara, S. Goto, J. Xu, T. Ito, J. Cryst. Growth **130**, 269 (1993)
24. Y.S. Chaudhary, S.A. Khan, R. Shrivastav, V.R. Satsangi, S. Prakash, D.K. Avasthi, S. Dass, Nucl. Instrum. Methods B **225**, 291 (2004)
25. Y.S. Chaudhary, S.A. Khan, R. Shrivastav, V.R. Satsangi, S. Prakash, U.K. Tiwari, D.K. Avasthi, N. Goswami, S. Dass, Thin Solid Films **492**, 332 (2005)
26. S. Rani, N.K. Puri, S.C. Roy, M.C. Bhatnagar, D. Kanjilal, Nucl. Instrum. Methods B **266**, 1987 (2008)
27. B.D. Cullity, *Elements of X-ray Diffractions* (Addison-Wesley, Reading, MA, 1978)
28. S. Maniv, W.D. Westwood, E. Colombini, J. Vac. Sci. Technol. **20**, 162 (1982)
29. V. Bilgin, S. Kose, F. Atay, I. Akyur, Mater. Chem. Phys. **94**, 103 (2005)
30. J.B. Seon, S. Lee, J.M. Kim, H.D. Jeong, Chem. Mater. **21**, 604 (2009)
31. M.B. Ortuno-Lopez, J.J. Valenzuela-Jauregui, M. Sotelo-Lerma, A. Mendoza-Galvan, R. Ramirez-Bon, Thin Solid Films **429**, 34 (2003)
32. S. Hemon, F. Gourbilleau, Ch. Dufour, E. Paumier, E. Dooryhee, A. Rouanet, Nucl. Instr. Methods B **122**, 526 (1997)
33. A. Berthelot, S. Hemon, F. Gourbilleau, C. Dufour, B. Domenges, E. Paumier, Phil. Mag. A **80**, 2567 (2000)
34. L.L. Yang, Q.X. Zhao, M. Willander, J.H. Yang, I. Ivanov, J. Appl. Phys. **105**, 053503 (2009)
35. V.K. Miloslavskii, P.S. Pogrebniak, Phys. Status Solidi B **51**, K99 (1972)
36. A. Berthelot, C. Durfour, B. Domenges, E. Paumier, Nucl. Instr. Methods B **166–167**, 927 (2000)
37. F. Zhuge, L.P. Zhu, Z.Z. Ye, D.W. Ma, J.G. Lu, J.Y. Huang, F.Z. Wang, Z.G. Ji, Appl. Phys. Lett. **87**, 092103 (2005)
38. S. Tuzemena, G. Xiong, J. Wilkinson, B. Mischuck, K.B. Ucer, R.T. Williams, Physica B **308–310**, 1197 (2001)
39. A. Sharma, K.D. Verma, M. Varshney, A.P. Singh, Y. Kumar, S. Shrivastava, Y.K. Vijay, K. Asokan, R.J. Choudhary, R. Kumar, Adv. Sci. Lett. **4**, 501 (2011)
40. J. Madau, S.R. Morrison, *Chemical Sensing with Solid State Devices*, 1st edn. (Academic Press, Boston, 1989)
41. M. Takata, D. Tsubone, H. Yanagida, J. Am. Ceram. Soc. **59**, 4 (1976)
42. V.R. Shinde, T.P. Gujar, C.D. Lokhande, R.S. Man, S.H. Han, Mater. Sci. Eng., B **137**, 119 (2007)
43. I. Jimenez, M.A. Centeno, R. Scotti, F. Morazzoni, A. Cornet, J.R. Morante, J. Electrochem. Soc. **150**, H72 (2003)
44. I. Jimenez, M.A. Centeno, R. Scotti, F. Morazzoni, J. Arbiol, A. Cornet, J.R. Morante, J. Mater. Chem. **14**, 2412 (2004)
45. J.K. Dirksen, K. Duval, T.A. Ring, Sens. Actuators, B **80**, 106 (2001)